ACS APPLIED MATERIALS & INTERFACES

Research Article

Cite This: ACS Appl. Mater. Interfaces 2018, 10, 40740−40747

www.acsami.org

Record-Low and Anisotropic Thermal Conductivity of a Quasi-One-Dimensional Bulk $ZrTe_5$ Single Crystal

Jie Zhu,[†,‡,▽] Tianli Feng,[§,∥,▽] Scott Mills,[⊥] Peipei Wang,[#] Xuewang Wu,[†] Liyuan Zhang,[#] Sokrates T. Pantelides,[§,∥] Xu Du,[⊥] and Xiaojia Wang*[,†,¶]

[†]Department of Mechanical Engineering and [¶]Department of Electrical and Computer Engineering, University of Minnesota, Minneapolis, MinnesotaMN 55455, United States

[‡]Key Laboratory of Ocean Energy Utilization and Energy Conservation of Ministry of Education, Dalian University of Technology, Dalian, Liaoning 116024, China

[§]Department of Physics and Astronomy and Department of Electrical Engineering and Computer Science, Vanderbilt University, Nashville, Tennessee 37235, United States

[∥]Materials Science and Technology Division, Oak Ridge National Laboratory, Oak Ridge, Tennessee 37831, United States

[⊥]Department of Physics and Astronomy, Stony Brook University, Stony Brook, New York 11794, United States

[#]Department of Physics, Southern University of Science and Technology, Shenzhen, Guangdong 518055, China

Supporting Information

ABSTRACT: Zirconium pentatelluride ($ZrTe_5$) has recently attracted renewed interest owing to many of its newly discovered extraordinary physical properties, such as 2D and 3D topological-insulator behavior, pressure-induced superconductivity, Weyl semimetal behavior, Zeeman splitting, and resistivity anomaly. The quasi-one-dimensional structure of single-crystal $ZrTe_5$ also promises large anisotropy in its thermal properties, which have not yet been studied. In this work, via time-domain thermoreflectance measurements, $ZrTe_5$ single crystals are discovered to possess a record-low thermal conductivity along the *b*-axis (through-plane), as small as 0.33 ± 0.03 W m^{-1} K^{-1} at room temperature. This ultralow *b*-axis thermal conductivity is 12 times smaller than its *a*-axis thermal conductivity (4 ± 1 W m^{-1} K^{-1}) owing to the material's asymmetrical crystalline structure. First-principles calculations are further conducted to reveal the physical origins of the ultralow *b*-axis thermal conductivity, which can be attributed to: (1) the resonant bonding and strong lattice anharmonicity induced by electron lone pairs, (2) the weak interlayer van der Waals interactions, and (3) the heavy mass of Te atoms, which results in low phonon group velocity. This work sheds light on the design and engineering of high-efficiency thermal insulators for applications such as thermal barrier coatings, thermoelectrics, thermal energy storage, and thermal management.

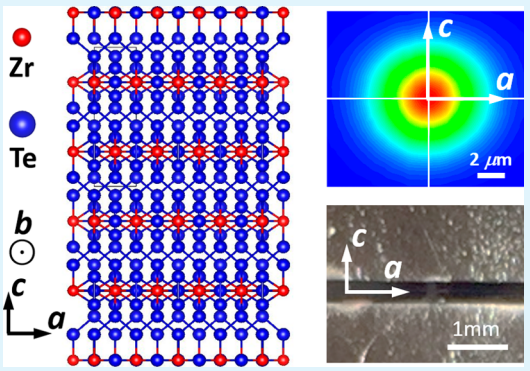

KEYWORDS: *ultralow thermal conductivity, quasi-one-dimensional material, anisotropic thermal transport, time-domain thermoreflectance, first-principles calculation*

Downloaded via VANDERBILT UNIV on February 20, 2019 at 02:39:48 (UTC).
See https://pubs.acs.org/sharingguidelines for options on how to legitimately share published articles.

1. INTRODUCTION

Recently, $ZrTe_5$ has drawn increasing attention as a functional material because of its distinct electronic,[1−6] optical,[7] and thermal properties[8−10] such as its resistivity anomaly and good thermoelectric performance.[11,12] $ZrTe_5$ is a layered material stacked along the *b*-axis. Each layer is composed of chains of $ZrTe_3$ prisms running along the *a*-axis, as shown in Figure 1. These prismatic chains are linked along the *c*-axis via zigzag Te chains to form 2D planes. Therefore, $ZrTe_5$ is a quasi-one-dimensional (quasi-1D) crystal. The weak van der Waals (vdW) force between layers makes it easy to mechanically exfoliate thin flakes of $ZrTe_5$. It has been found that this quasi-1D nature endows $ZrTe_5$ single crystals with significantly anisotropic electrical conductivity that has promising applications in electronics.[1,4,5]

Also associated with the quasi-1D nature, the thermal transport properties of the $ZrTe_5$ single crystal may offer intriguing opportunities for applications in thermal management in electronic devices. To date, the study of thermal transport in $ZrTe_5$ has been limited to alloys and polycrystals. A few experimental works have reported varying values ranging from 1.5 to 8 W m^{-1} K^{-1}.[9,11−13] Most of the values were averaged along different crystalline orientations as the samples

Received: July 24, 2018
Accepted: November 2, 2018
Published: November 2, 2018

© 2018 American Chemical Society

DOI: 10.1021/acsami.8b12504
ACS Appl. Mater. Interfaces 2018, 10, 40740−40747

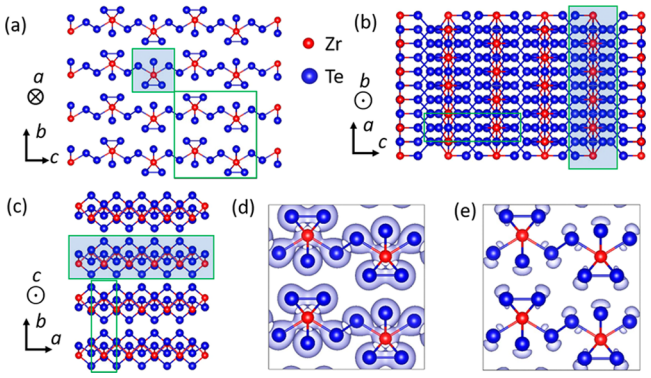

Figure 1. (a–c) Lattice structures of $ZrTe_5$ as viewed against the crystalline *a*, *b*, and *c* axes. The open green boxes indicate unit cells. The shaded green boxes highlight the 1D chains. (d) Electron density and (e) localization function (ELF) isosurfaces at ELF = 0.88 calculated using density functional theory.

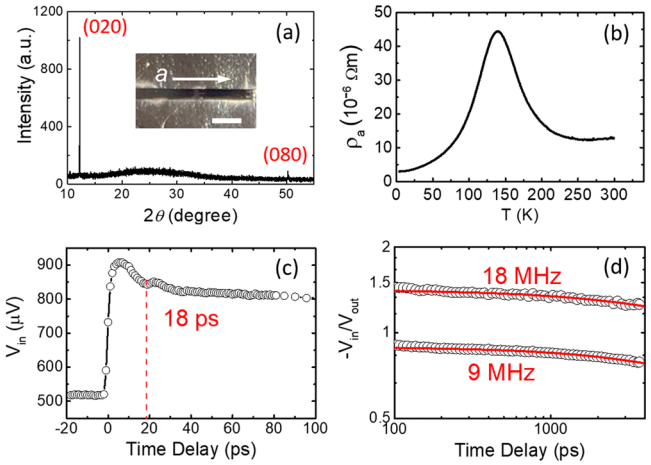

Figure 2. $ZrTe_5$ single-crystal and through-plane TDTR measurements. (a) XRD data. The inset is a photo image of S-3. The scale bar is 1 mm; (b) temperature dependence of resistivity along the *a*-axis, where a peak at 140 K is observed, which is induced by the Lifshitz transition; (c) TDTR in-phase signals for determining Al thickness with picosecond acoustics. The first echo at 18 ps indicates an Al thickness of 58 nm; (d) TDTR ratio signals (open circles) at f_m = 18 and 9 MHz with the corresponding best-fit curves (red solid lines).

were polycrystalline or alloyed.[11,12] There exists one experimental study of single-crystal $ZrTe_5$ along the *a*-axis (8 W m^{-1} K^{-1}).[9] However, this anomalously high value was considered to have a significant error by other researchers.[11] Thus, the anisotropic thermal conductivity of single crystals remains elusive. More importantly, the previously measured values of $ZrTe_5$ polycrystals and alloys contain substantial electronic contributions and the effects of many unknown defects and grain boundaries on the phononic contribution. Therefore, the intrinsic lattice thermal conductivity of $ZrTe_5$ may deviate significantly from these reported values. On the other hand, although a few theoretical works have calculated the thermal conductivity of $ZrTe_5$,[14,15] the anisotropy has not been studied yet.

In this study, we focus on the anisotropic thermal transport in high-quality, bulk, single-crystal $ZrTe_5$ along both the basal-plane and through-plane directions. Our approach integrates theoretical and experimental investigations, revealing the fundamental mechanisms of the anisotropic thermal transport in $ZrTe_5$. To achieve this objective, we synthesized large-size high-quality $ZrTe_5$ crystals and employed the technique of ultrafast time-domain thermoreflectance (TDTR) to study their intrinsic anisotropic three-dimensional thermal conductivities. We found a record-low thermal conductivity (0.33 W m^{-1} K^{-1}) along the through-plane direction (*b* axis) of single-crystal $ZrTe_5$. To provide physical insights into the experimental work, first-principles calculations have been performed for bulk $ZrTe_5$ crystals to reveal the characteristics of thermal transport along both the in-plane and through-plane directions. Excellent agreement has been achieved between theoretical and experimental results regarding the thermal conductivities of $ZrTe_5$ along different crystal orientations. The origin of the poor thermal transport across the $ZrTe_5$ layers has been revealed by using the theoretical predictions.

2. RESULTS

2.1. Structural Characterization of $ZrTe_5$. $ZrTe_5$ single crystals were synthesized with the chemical vapor transport (CVT) method, which produced ribbon-shaped single crystals with a typical size of ~0.6 mm × 0.6 mm × 5 mm (Figure 2a inset). Figure 2a shows the X-ray diffraction (XRD) spectrum of such a $ZrTe_5$ crystal, where sharp peaks along the (020) and (080) directions are clearly visible. The quality of the single crystals is better characterized through the temperature dependence of the resistivity along the *a*-axis as shown in Figure 2b, where a peak at 140 K is observed, induced by the Lifshitz transition.[5] The peak position observed here is within the typical range of T_p = 120–150 K for CVT-synthesized high-quality $ZrTe_5$ single crystals.[5,16]

2.2. Through-Plane Thermal Conductivity Measurements. Three $ZrTe_5$ flakes have been measured in this work, labeled S-1, S-2, and S-3. For S-1 and S-2 $ZrTe_5$ flakes, thin transducer films (58 and 52 nm, respectively) of aluminum (Al) were deposited for both in-plane and through-plane thermal measurements, whereas an Al transducer with a typical thickness of 80 nm was coated on sample S-3 for through-plane TDTR experiments only.

In TDTR measurements, a mode-locked Ti:sapphire laser serves as the light source, which produces a train of pulses (~100 fs) at a repetition rate of 80 MHz. The laser is split into a pump beam and a probe beam through a polarizing beam splitter. The pump beam is modulated as a sinusoidal wave by an electro-optical modulator at a modulation frequency of f_m. A mechanical delay stage varies the optical path of the pump beam, producing a time delay of up to ~4 ns between the pump excitation and probe sensing. An objective lens is used to focus both the pump and probe beams on the sample surface with a beam spot size ($1/e^2$ radius) from 3 to 12 μm. The in-phase (V_{in}) and out-of-phase (V_{out}) signals are collected by a photodetector and then an rf lock-in amplifier to the computer for data analysis. The ratio of signals ($-V_{in}/V_{out}$) is compared with a thermal model to extract the unknown thermal properties.[17−19] The Al transducer thickness can be determined simultaneously from picosecond acoustics during TDTR measurements.[20,21] Figure 2c shows a representative picosecond acoustic signal of S-1, and the first echo at 18 ps gives 58 nm as the Al transducer thickness. The acoustic impedance data are detailed in the Supporting Information.

Multi-frequency through-plane TDTR measurements have been conducted on all three samples.[22,23] A heat capacity of 1.27 MJ m^{-3} K^{-1} is used for $ZrTe_5$ crystals in the data analysis.[24] The obtained through-plane (along the *b* axis)

DOI: 10.1021/acsami.8b12504
ACS Appl. Mater. Interfaces 2018, 10, 40740−40747

thermal conductivities (Λ_b) are 0.30 ± 0.02, 0.33 ± 0.03, and 0.35 ± 0.03 W m^{-1} K^{-1} for S-1, S-2, and S-3, respectively. The variation among these results for different samples falls within the 8% uncertainty of TDTR measurements, indicating good consistency in the measurements of different samples with varying Al-transducer thicknesses. The averaged Λ_b of 0.33 ± 0.03 W m^{-1} K^{-1} at room temperature is the record-low thermal conductivity value for single crystals. To date, the experimentally reported lowest thermal conductivity of single-crystal materials in literature is 0.46 W m^{-1} K^{-1}, along the *a*-axis of SnSe,[25] which was, however, partially attributed to the possibly existing porosity of the sample.[26] The thermal conductivities of all other single crystals that have been reported to possess low thermal conductivities, for example, β-$Zn_{13}Sb_{10}$ (0.85 W m^{-1} K^{-1})[27] and Bi_2Te_3 (0.76 W m^{-1} K^{-1}),[28] are all higher than 0.7 W m^{-1} K^{-1}.

The representative TDTR signals and fitting curves at modulation frequencies of 18 and 9 MHz for sample S-1 are shown in Figure 2d. The interfacial thermal conductance between the Al film and $ZrTe_5$ is within the range of 7−11 MW m^{-2} K^{-1} for all three samples, suggesting a relatively weaker interfacial thermal transport between Al and $ZrTe_5$ than that typically between a metal and a semiconductor. In addition, we took scanning electron microscope (SEM) images to see the area of the Al/$ZrTe_5$ interface. We did not see a clear visible contrast at the Al/$ZrTe_5$ interface in the SEM images (Figure S1 in the Supporting Information), which indicates there is no significant Al atom diffusion into $ZrTe_5$. This is in contrast to previous work showing that metal atoms, such as Pd, can diffuse into $ZrTe_5$ crystals when they are in contact,[7] and other metal atoms (e.g., Cu, Ni, Co, or Fe) diffuse into topological insulators (e.g., Bi_2Se_3)[29] and thermoelectric materials (e.g., Bi_2Te_3).[30]

2.3. In-Plane Thermal Conductivity Measurements. To obtain the in-plane thermal conductivity of $ZrTe_5$, we conducted 2D in-plane scanning using the beam-offset approach.[31−33] During the experiments, the sample was mounted with the *a*-axis along the vertical direction. Figure 3a illustrates a charge-coupled device (CCD) image of sample S-2 with a 20× objective lens (beam spot size of ∼3 μm), which suggests a sufficiently large and smooth area of the sample surface for the beam-offset measurements.

From a sensitivity analysis detailed in Figure S2 of the Supporting Information, we find that the thermal conductivity of the Al transducer has a strong influence on the beam-offset signals. Thus, using accurate thermal properties of the transducer layer for the data analysis is essential to obtain reliable in-plane thermal conductivity of $ZrTe_5$ in the present experiments. Therefore, prior to the beam-offset measurements of $ZrTe_5$ samples, we characterized the thermal properties of the Al transducer by measuring the Al/SiO_2 reference samples, which were placed next to the $ZrTe_5$ samples during the Al sputtering deposition. The thermal properties of Al were obtained from both the through-plane and in-plane TDTR measurements of these reference samples. With a known thermal conductivity of SiO_2 (1.4 W m^{-1} K^{-1}, as previously verified for the same wafer), we obtained the in-plane thermal conductivity of the Al transducer to be 76 ± 3 W m^{-1} K^{-1} as averaged over three locations of each sample. This value of the Al thin-film transducer is much lower than that of bulk Al (237 W m^{-1} K^{-1}).[34] The volumetric heat capacity of the Al transducer was also determined to be 2.23 ± 0.04 MJ m^{-3} K^{-1} from through-plane TDTR measurements of the Al/SiO_2 reference samples, which is slightly lower (∼9%) than the bulk value (2.42 MJ m^{-3} K^{-1}). These thermal properties of the Al transducer extracted from measurements of reference samples were later used as input parameters in the data analysis of in-plane beam-offset measurements of $ZrTe_5$, allowing accurate determination of the sample thermal properties as demonstrated in literature.[33,35]

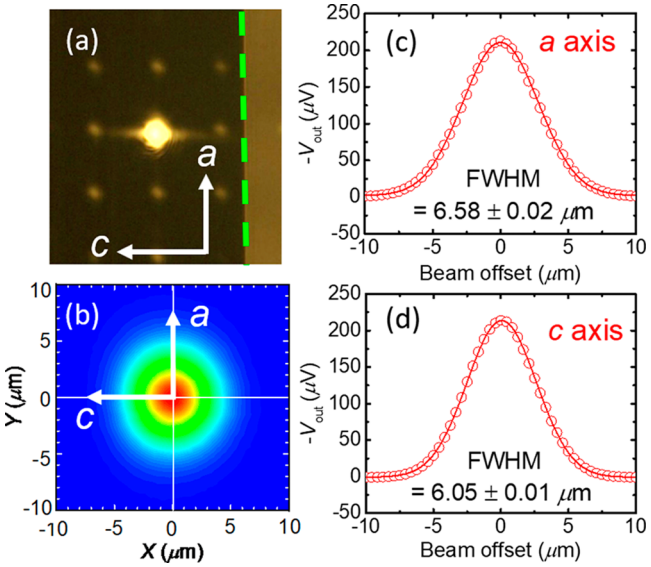

Figure 3. In-plane thermal measurements on $ZrTe_5$ using the beam-offset method. (a) 20× microscopic CCD image of sample S-2 with a laser beam spot of ∼3 μm. The *a*-axis is along the vertical direction and the dashed green line represents the edge of the sample flake; (b) Two-directional beam-offset signal ($-V_{out}$) contour of sample S-2; (c,d) represent the beam-offset signals along the *a* and *c* crystal orientations, respectively, taken from the 2D contour in (b). The fitting errors in the full width at half maximum are estimated to be less than 0.3%.

The 2D contour plots of the out-of-phase signals (V_{out}) measured by in-plane beam-offset TDTR are illustrated in Figure 3b for sample S-2, of which the *X*-axis is along the *c*-axis of the $ZrTe_5$ flake. The measurements were conducted at a fixed time delay of −50 ps. Results from this 2D-scanning method generate a contour plot that can be used to extract the in-plane thermal conductivity of $ZrTe_5$ along any crystalline direction. This method also provides a straightforward manner to accurately determine the primary crystalline directions from post-data processing, eliminating the need to align the sample loading along a certain crystalline orientation for thermal measurements, which can be challenging and time-consuming. Corrections on V_{out} mapping signals are made as we detailed in a previous work.[33] These corrections are essential for processing the measurement data to obtain accurate thermal properties of the sample.

The in-plane thermal conductivity is obtained by comparing the full width at half-maximum (fwhm) of V_{out} along the *X* or *Y* direction with the calculated values from the thermal model.[17,31] Figure 3c,d shows the beam-offset signals along the *a* and *c* crystal orientations that are extracted from the 2D contour in Figure 3b. The in-plane thermal conductivity of $ZrTe_5$ along the *Y* direction, which corresponds to the *a*-axis of sample S-2, is found to be Λ_a = 4.2 W m^{-1} K^{-1}, averaged by four measurements on different locations of S-2. An accurate determination of the *c*-axis thermal conductivity has been prohibited by the poor sensitivity of the beam-offset signals

DOI: 10.1021/acsami.8b12504
ACS Appl. Mater. Interfaces 2018, 10, 40740−40747

along this direction, presumably because of the lower *c*-axis thermal conductivity compared to that along the *a*-axis. This speculation is consistent with the first-principles calculation results described in Section 3. Using the same approach, we obtain the Λ_a of sample S-1 as 3.8 W m^{-1} K^{-1}. Therefore, the averaged Λ_a = 4 ± 1 W m^{-1} K^{-1}, which gives an anisotropy ratio of $\Lambda_a/\Lambda_b \approx 12$ between the *a* and *b* axes.

3. THEORETICAL PREDICTIONS

To understand the physical origins of the anisotropic thermal transport and especially the record-low thermal conductivity along the through-plane direction in single-crystal bulk $ZrTe_5$, we have performed comprehensive first-principles density functional theory (DFT) calculations.

Our work uses the standard DFT calculations without an extra vdW functional. We note that ref 14 predicted the thermal conductivities of 8.6, 7.4, 7.2 W m^{-1} K^{-1} for *a*, *b*, and *c* directions by using DFT with an extra vdW functional. Prior studies of the thermal conductivity of vdW crystals such as multilayer graphene, graphite, and Bi_2Te_3 have demonstrated that calculation results from the standard DFT agreed well (or even better) with experimental data, when the vdW functional was excluded.[36−38] We have examined the relaxed lattice constant from DFT calculations with and without the vdW functional, and we find that they both give reasonable agreement with experiment results (see details in Table S2 of the Supporting Information).

The DFT-calculated electron density and localization function are shown in Figure 1d,e, respectively. It is seen that the interlayer gap has weak wavefunction overlap, indicating weak vdW interactions. This is consistent with the small through-plane phonon velocity that will be discussed later. The electron localization function profile indicates that electron lone pairs exist in Te atoms so that the bonding between Zr and Te is resonant,[39] which can lead to large lattice anharmonicity and low thermal conductivity. This feature will be further confirmed by the strong anharmonic phonon scattering.

The DFT-calculated phonon dispersion relation is shown in Figure 4a. Surprisingly, we find that most of the optical phonon branches along the *b*-axis (Γ−*Y*) are nearly flat, which indicates that their group velocities are nearly 0, that is, they are almost standing waves and contribute little to direct heat conduction. This result is consistent with the weak vdW interlayer interaction observed in the electron density (wave function overlaps) shown in Figure 1d. We also note that the acoustic phonons along the *b*-axis (Γ−*Y*) have very small group velocities. The calculated total and projected phonon densities of states (DOS) are shown in Figure 4b. We find that the Zr and Te atoms have distinct contributions to the lattice vibrations. The Zr atoms predominantly contribute to the high-energy (>5.5 THz) optical modes because of their lighter atomic mass, whereas the Te atoms dominate the acoustic phonons as well as all the low-energy optical phonons (<5.5 THz) because of their large stoichiometric ratio and heavier atomic mass. Such distinct contributions support the observation of resonant bonding, similar to that in PbS.[39,40] Later, we show that the high-energy (>5.5 THz) optical modes contribute negligibly to the lattice thermal conductivity, which suggests that the Te atoms dominate the heat conduction, whereas the vibrations of Zr atoms make no substantial contribution to the lattice thermal conductivity.

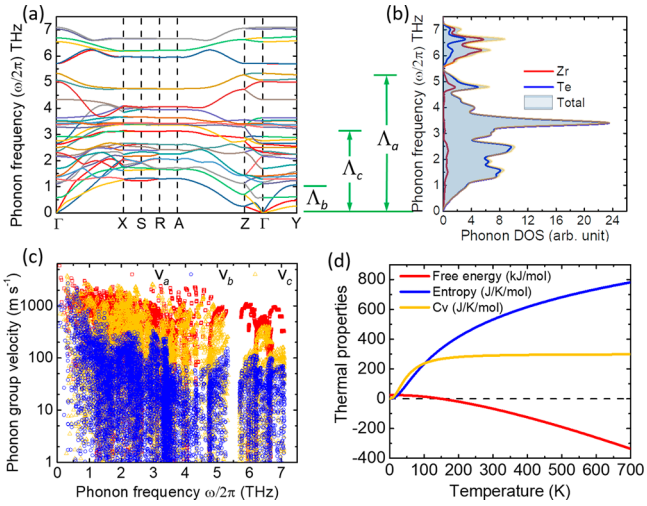

Figure 4. (a) DFT-calculated phonon dispersion relation along high-symmetry directions. (b) Total and projected phonon densities of states. The dominant phonon frequencies for Λ_a, Λ_b, and Λ_c are shown in between (a,b). (c) Phonon group velocity spectra along the *a*, *b*, and *c* axes. (d) Heat capacity, entropy, and free energy as functions of temperature.

Figure 4c depicts the phonon group velocities (ν_g) calculated along the *a*, *b*, and *c* crystalline directions. It can be clearly seen from Figure 4c that the phonon group velocities along the *b*-axis are significantly smaller than those along the *c*-axis, which are yet smaller than those along the *a*-axis. These results are consistent with the quasi-1D atomic structure of $ZrTe_5$, which has the weakest bonding along *b* and strongest along *a*. The velocities of the near-Γ acoustic phonons are 2217, 494, and 2185 m s^{-1}, respectively, along Γ−*X*, Γ−*Y*, and Γ−*Z*. The corresponding Debye temperatures calculated by $\Theta_D = (h\nu_g)/k_B(3n/4\pi)^{(1/3)}$ with *n* being the atomic density and *h* being the Plank constant are 209, 46, and 206 K, respectively, along these three directions. From phonon spectra, thermal properties such as the heat capacity, entropy, and free energy are calculated, as shown in Figure 4d. From the convergence trend of the temperature-dependent heat capacity, Θ_D of $ZrTe_5$ is determined to be ∼150 K, consistent with the average of the values associated with each of the three directions (154 K).

To gain some insights into the anharmonicity, we calculate the Grüneisen parameter, three-phonon scattering rates, and relaxation times over a range of phonon frequencies, as shown in Figure 5a−c, respectively. The Grüneisen parameter above Θ_D (∼150 K) converges at 1.25, close to the values of ultralow thermal conductivity resonant-bonding materials calculated from DFT in literature, such as SnSe (1.41) and Bi_2Te_3 (1.5).[25,41] A full comparison is included in Table S1 of the Supporting Information. This indicates that the anharmonicity of $ZrTe_5$ could be very large, which is consistent with what the electron localization function in Figure 1e suggests: the electron lone pairs result in resonant bonding and strong anharmonicity. The large three-phonon scattering rates and short relaxation times shown in Figure 5b,c again support the large anharmonicity.

With these results, we have obtained the room-temperature thermal conductivities (Figure 5f) along the *a*, *b*, and *c* directions, which are 3.9, 0.36, and 1.9 W m^{-1} K^{-1}, respectively, and agree excellently with experimental results. The anisotropy ratio between the *a* and *b* axes is as high as 11, whereas the in-plane anisotropy ratio between the *a* and *c* axes

DOI: 10.1021/acsami.8b12504
ACS Appl. Mater. Interfaces 2018, 10, 40740−40747

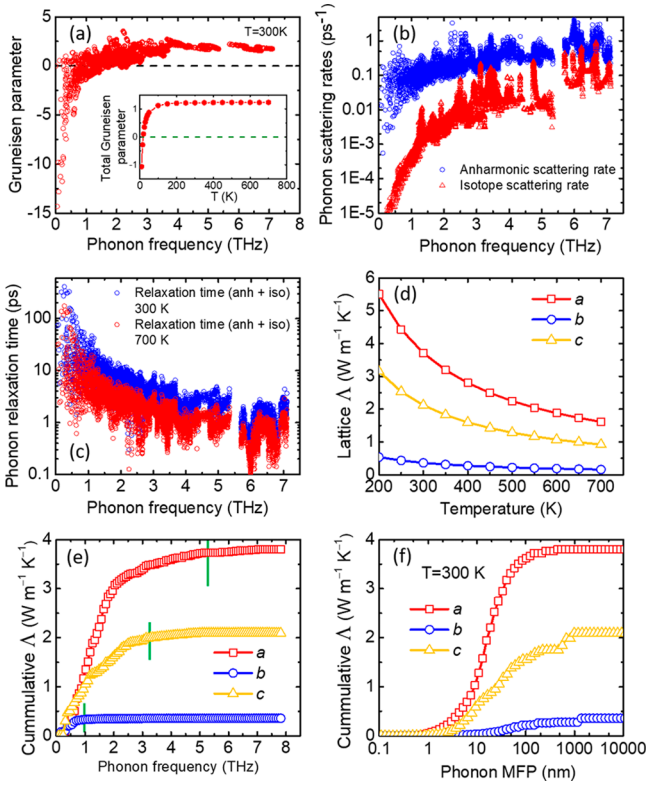

Figure 5. (a) Frequency-dependent room-temperature Grüneisen parameter spectra. The inset shows the temperature-dependent total Grüneisen parameter. (b) Frequency-dependent three-phonon and phonon-isotope scattering rates spectra. (c) Phonon relation time spectra at 300 and 700 K. (d) DFT-calculated temperature-dependent thermal conductivities along the *a*, *b*, and *c* axes. (e,f) Cumulative thermal conductivity as a function of phonon frequency and mean free path.

is around 2. We also note here that the thermal conductivity along the *c*-axis is indeed lower than that of the *a*-axis. This result supports our speculation on why we cannot obtain a certain value along the *c*-axis through our beam-offset measurements. Further explanations are provided with the sensitivity analysis detailed in Figure S2 of the Supporting Information.

To gain some physical interpretation of measurement results, we calculate the cumulative phonon thermal conductivities as functions of phonon frequency and mean free path, which are shown in Figure 5e,f, respectively. It is clearly seen that the thermal conductivities along the *a*, *b*, and *c* directions are contributed by the phonon modes with frequencies (and thus energies) lower than 1, 3, and 5.5 THz, respectively. The high-energy phonons with frequencies above 5.5 THz do not contribute much to the heat conduction in any direction because they have the shortest relaxation times and small group velocities. Moreover, we have found that the three acoustic branches contribute 43% to the in-plane thermal conductivities (Λ_a and Λ_c), and the 33 optical branches contribute the remaining 57%. In contrast, the three acoustic branches contribute 94% to the through-plane thermal conductivity Λ_b, and the 33 optical branches contribute only the remaining 6%. This result is consistent with the observed nearly flat dispersion curves shown in Figure 4a, which indicates standing-wave-like optical phonons that transport little or no energy. The mean-free-path spectra illustrate that the most significant phonons that dominate thermal transport have mean free paths shorter than 100 nm. This information is important for nanoengineering as it provides the guidance to manipulate the most significant phonons. We note that, interestingly, although the through-plane direction has the lowest thermal conductivity, it contains the longest phonon mean free path (MFP). This behavior has been observed in other vdW crystals such as graphite.[42]

The DFT calculations have allowed us to unveil the physical origins of the ultralow through-plane thermal conductivity of $ZrTe_5$ single crystals: (1) the electron lone pairs of Te atoms lead to resonant bonding and strong lattice anharmonicity, (2) the weak interlayer vdW interaction leads to slow acoustic phonons and nearly flat optical phonon branches along the through-plane direction, and (3) the heavy mass of Te leads to low phonon frequencies and small group velocities.

In the following, we discuss the comparison between our thermal conductivity and the experimental data in literature. There is only one set of published data available for single-crystal $ZrTe_5$ thermal measurements,[9] which, however, were questionable as pointed out by ref 11 because of the small size and needle-like shape of the single crystals. For the comparison with polycrystals in literature, there are two simplified ways to average the thermal conductivity, namely, arithmetic $\Lambda = (\Lambda_a + \Lambda_b + \Lambda_c)/3$ and harmonic $1/\Lambda = (1/\Lambda_a + 1/\Lambda_b + 1/\Lambda_c)/3$.[43] Using our measured anisotropic thermal conductivity of single-crystal $ZrTe_5$, the arithmetic average gives ~2 W m^{-1} K^{-1} and the harmonic average gives 0.73 W m^{-1} K^{-1} for polycrystalline $ZrTe_5$. We consider these to be the upper and lower limits. The thermal conductivity was reported to be ~1.5 W m^{-1} K^{-1} in ref 11, which is in between the arithmetic and harmonic averages. Another issue is that for the polycrystalline samples in literature, there might be also a bipolar contribution to thermal conductivity. For example, the thermal conductivity of 1.5 W m^{-1} K^{-1} reported in ref 11 contains contributions from both lattice and bipolar as suggested by Figure 4d of ref 11. If the bipolar contribution is subtracted, the lattice thermal conductivity can be smaller than 1.5 W m^{-1} K^{-1}, closer to the lower limit of the harmonic average. Similarly, ref 12 measured a thermal conductivity of ~2 W m^{-1} K^{-1} at room temperature with negligible electronic contribution. However, their temperature-dependent thermal conductivity shows an increasing trend, instead of the typical $1/T$ dependence, for room temperature and beyond (Figure 3a in ref 12). We suspect it is likely caused by the bipolar contribution as described in ref 11.

4. CONCLUSIONS

In summary, we have conducted both experimental and theoretical studies on the anisotropic thermal conductivities of single-crystalline $ZrTe_5$. Three sample flakes were prepared for TDTR thermal measurements. We found that the *b*-axis thermal conductivity of the $ZrTe_5$ single crystal is as small as 0.33 ± 0.03 W m^{-1} K^{-1} at room temperature, which is a record-low thermal conductivity value for single crystals. The *a*-axis thermal conductivity is measured as 4 ± 1 W m^{-1} K^{-1}, giving an anisotropic ratio of $\Lambda_a/\Lambda_b \approx 12$. DFT calculations predict the room-temperature thermal conductivities along *a*, *b* and *c* directions as 3.9, 0.36, and 1.9 W m^{-1} K^{-1}, respectively, which agree excellently with experiment results. The physical origins of the ultralow through-plane thermal conductivity are attributed to: (1) the resonant bonding and strong lattice anharmonicity induced by electron lone pairs of Te atoms, (2) the slow acoustic phonons because of weak interlayer vdW

DOI: 10.1021/acsami.8b12504
ACS Appl. Mater. Interfaces 2018, 10, 40740−40747

interaction, and (3) the low phonon frequencies and group velocities because of the heavy mass of Te. These may shed light on the discovery and construction of ultralow thermal conductivity materials for applications such as thermal barrier coating, thermoelectrics, thermal storage, and thermal management.

5. EXPERIMENTAL SECTION

5.1. Sample Preparation. $ZrTe_5$ single crystals were synthesized by the CVT method, with iodine as transport agency. Stoichiometric proportions of Zr(3N) and Te(5N) powders, together with 5 mg mL^{-1} I_2, were loaded into a quartz tube under argon atmosphere. The quartz tube was flame-sealed and then placed in a two-zone furnace, where a temperature gradient from 480 to 400 °C was applied. After 4 weeks of reaction, golden, ribbon-shaped single crystals were formed with a typical size of about 0.6 mm × 0.6 mm × 5 mm.

5.2. Deposition and Characterization of the Al Transducer. In this work, Al films (~60 nm thick) were deposited on $ZrTe_5$ samples by rf sputtering (AJA sputtering system ATC 2200) to serve as metal transducers in TDTR measurements. Small deposition rates ($\leq$1 nm min^{-1}) were used during the sputtering, resulting in lowered thermal conductivity of the Al films. This feature can enhance the beam-offset measurement sensitivity to the in-plane thermal transport. The thickness of the Al transducer was determined from picosecond acoustics of the TDTR in-phase signal, and the volumetric heat capacity was taken from literature.[44] To better characterize the transducer, a 300 nm SiO_2 reference sample was also coated with the Al transducer in the same batch with each $ZrTe_5$ sample. The thermal conductivity and volumetric specific heat of Al were determined from TDTR measurements on the reference SiO_2 sample with known thermophysical properties, as what was done previously.[33]

5.3. Electrical Conductivity Measurements. The electrical conductivity measurements were carried out on bulk single-crystal $ZrTe_5$. To enhance the electrical contact, a thin layer of Au was evaporated through a mask onto four isolated spots. Gold wires were then attached to these spots with silver paste, forming the electrodes for standard four-probe measurements. The sample was cooled down in an Oxford Variable Temperature Insert (VTI). Standard four-terminal resistance measurements were carried out using a lock-in amplifier. The resistivity was then calculated using the measured electrical resistance and the dimensions of the sample device. Because of the small size of our synthesized needle-like $ZrTe_5$ single crystals, only the resistivity along the *a*-axis was obtained.

5.4. Thermal Conductivity Measurements. In through-plane TDTR measurements, a 5× objective lens was used to focus the pump and probe beams, producing the spot radii that were ~11 to 12 μm. The modulation frequencies were set as 9 and 18 MHz. The final results were averaged using measurements from three different locations. However, for the in-plane TDTR measurements, a 20× objective lens was used to produce a much smaller spot radius of ~3 μm. In both through-plane and in-plane measurements, the beam spot size was accurately characterized with the beam-offset method at 30 ps delay time to reduce the measurement uncertainty.[33] A delay time of −50 ps and a modulation frequency of 1.6 MHz were used for the in-plane beam-offset thermal measurements.

5.5. First-Principles Calculations. First-principles calculations were carried out with the VASP program package[45,46] using the projector augmented wave method[46] in the local density approximation for exchange−correlation effects. The atoms in the unit cell (composed of two primitive unit cells) were relaxed using a convergence threshold of 10^{-7} eV for the total energy and 10^{-7} eV $Å^{-1}$ for the forces on each atom. The plane-wave energy cutoff was 400 eV. The electronic *k*-space integration was performed with the tetrahedron method, involving a 12 × 6 × 4 Monkhorst−Pack *k*-mesh. The relaxed lattice constants along *a*, *b*, and *c* were 3.94, 14.26, and 13.53 Å, which fall within a few percent of the experimental values of 3.86−3.99, 14.47−14.53, 13.68−13.72 Å, respectively.[8,10,47,48] Spin−orbit coupling was not included as it is not critical for lattice vibration properties, and it would extremely increase the computational cost. The lattice constants from experiments as well as from different electronic methods in DFT are summarized in Table S2 of the Supporting Information. The phonon dispersion was calculated via 3 × 2 × 2 unit cells (288 atoms) by the finite displacement method using the PHONOPY package[49] with a 4 × 3 × 2 Monkhorst−Pack *k*-mesh. The thermal conductivity was calculated by the exact solution to the linearized Boltzmann transport equation that is implemented in the ShengBTE package with the detailed formalism and algorithms shown in ref 50. The third-order force constants are calculated by including up to the sixth nearest neighbors. The calculation used a 20 × 6 × 6 *q*-mesh. The thermal conductivity convergence with respect to the *q*-mesh is shown in Figure S3 of the Supporting Information.

■ ASSOCIATED CONTENT

Supporting Information

The Supporting Information is available free of charge on the ACS Publications website at DOI: 10.1021/acsami.8b12504.

Details regarding the experimental characterization and measurements, including the impedance calculation, sample microscopic images, and thermal measurement sensitivity analysis; and the convergence study and material parameters related to the first-principles calculations (PDF)

■ AUTHOR INFORMATION

Corresponding Author

*E-mail: wang4940@umn.edu.

ORCID

Xu Du: 0000-0001-5610-2338

Xiaojia Wang: 0000-0001-7612-1739

Author Contributions

[▽]J.Z. and T.L.F. contributed equally to this paper.

Notes

The authors declare no competing financial interest.

■ ACKNOWLEDGMENTS

This work was supported by the National Science Foundation (NSF) through the University of Minnesota MRSEC under Award number DMR-1420013 and partially by the Legislative-Citizen Commission on Minnesota Resources and the Institute on the Environment. X.W. thanks the support from NSF (1804840). J.Z. would like to thank the support from the National Natural Science Foundation of China (grant no. 51336009). Work at Vanderbilt (T.L.F., S.T.P.) was supported in part by the Department of Energy grant DE-FG0209ER46554 and by the McMinn Endowment. Computations at Vanderbilt University and ORNL were performed at the National Energy Research Scientific Computing Center (NERSC), a Department of Energy, Office of Science, User Facility funded through contract no. DE-AC02-05CH11231. Computations also used the Extreme Science and Engineering Discovery Environment (XSEDE). X.D. and L.Z. acknowledge support from Guangdong Innovative and Entrepreneurial Research Team Program (no. 2016ZT06D348) and Shenzhen Fundamental subject research program (JCYJ20170817110751776) and free exploration (JCYJ20170307105434022). X.D. would also like to acknowledge Philip Allen for insightful discussions, and Fernando Camino for the help in characterizing the cross sections of the $ZrTe_5$ crystals. This research used resources of the Center for Functional Nanomaterials, which is a US DOE Office of

DOI: 10.1021/acsami.8b12504
ACS Appl. Mater. Interfaces 2018, 10, 40740−40747

Science Facility, at Brookhaven National Laboratory under contract no. DE-SC0012704.

REFERENCES

(1) Manzoni, G.; Sterzi, A.; Crepaldi, A.; Diego, M.; Cilento, F.; Zacchigna, M.; Bugnon, P.; Berger, H.; Magrez, A.; Grioni, M.; Parmigiani, F. Ultrafast Optical Control of the Electronic Properties of $ZrTe_5$. *Phys. Rev. Lett.* **2015**, *115*, 207402.

(2) Weng, H.; Dai, X.; Fang, Z. Transition-Metal Pentatelluride $ZrTe_5$ and $HfTe_5$: A Paradigm for Large-Gap Quantum Spin Hall Insulators. *Phys. Rev. X* **2014**, *4*, 011002.

(3) Chen, R. Y.; Chen, Z. G.; Song, X.-Y.; Schneeloch, J. A.; Gu, G. D.; Wang, F.; Wang, N. L. Magnetoinfrared Spectroscopy of Landau Levels and Zeeman Splitting of Three-Dimensional Massless Dirac Fermions in $ZrTe_5$. *Phys. Rev. Lett.* **2015**, *115*, 176404.

(4) Li, X.-B.; Huang, W.-K.; Lv, Y.-Y.; Zhang, K.-W.; Yang, C.-L.; Zhang, B.-B.; Chen, Y. B.; Yao, S.-H.; Zhou, J.; Lu, M.-H.; Sheng, L.; Li, S.-C.; Jia, J.-F.; Xue, Q.-K.; Chen, Y.-F.; Xing, D.-Y. Experimental Observation of Topological Edge States at the Surface Step Edge of the Topological Insulator $ZrTe_5$. *Phys. Rev. Lett.* **2016**, *116*, 176803.

(5) Zhang, Y.; Wang, C.; Yu, L.; Liu, G.; Liang, A.; Huang, J.; Nie, S.; Sun, X.; Zhang, Y.; Shen, B.; Liu, J.; Weng, H.; Zhao, L.; Chen, G.; Jia, X.; Hu, C.; Ding, Y.; Zhao, W.; Gao, Q.; Li, C.; He, S.; Zhao, L.; Zhang, F.; Zhang, S.; Yang, F.; Wang, Z.; Peng, Q.; Dai, X.; Fang, Z.; Xu, Z.; Chen, C.; Zhou, X. J. Electronic Evidence of Temperature-Induced Lifshitz Transition and Topological Nature in $ZrTe_5$. *Nat. Commun.* **2017**, *8*, 15512.

(6) Li, Q.; Kharzeev, D. E.; Zhang, C.; Huang, Y.; Pletikosić, I.; Fedorov, A. V.; Zhong, R. D.; Schneeloch, J. A.; Gu, G. D.; Valla, T. Chiral Magnetic Effect in $ZrTe_5$. *Nat. Phys.* **2016**, *12*, 550−554.

(7) Léonard, F.; Yu, W.; Collins, K. C.; Medlin, D. L.; Sugar, J. D.; Talin, A. A.; Pan, W. Strong Photothermoelectric Response and Contact Reactivity of the Dirac Semimetal $ZrTe_5$. *ACS Appl. Mater. Interfaces* **2017**, *9*, 37041−37047.

(8) Littleton, R. T., IV; Tritt, T. M.; Kolis, J. W.; Ketchum, D. R. Transition-Metal Pentatellurides as Potential Low-Temperature Thermoelectric Refrigeration Materials. *Phys. Rev. B: Condens. Matter Mater. Phys.* **1999**, *60*, 13453−13457.

(9) Zawilski, B. M.; Littleton, R. T., IV; Tritt, T. M. Investigation of the Thermal Conductivity of the Mixed Pentatellurides $Hf_{1-X}Zr_XTe_5$. *Appl. Phys. Lett.* **2000**, *77*, 2319−2321.

(10) Littleton, R. T., IV; Tritt, T. M.; Kolis, J. W.; Ketchum, D. R.; Lowhorn, N. D.; Korzenski, M. B. Suppression of the Resistivity Anomaly and Corresponding Thermopower Behavior in the Pentatelluride System by the Addition of Sb: $Hf_{1-X}Zr_XTe_{5-Y}Sb_Y$. *Phys. Rev. B* **2001**, *64*, 121104.

(11) Miller, S. A.; Witting, I.; Aydemir, U.; Peng, L.; Rettie, A. J. E.; Gorai, P.; Chung, D. Y.; Kanatzidis, M. G.; Grayson, M.; Stevanović, V.; Toberer, E. S.; Snyder, G. J. Polycrystalline $ZrTe_5$ Parametrized as a Narrow-Band-Gap Semiconductor for Thermoelectric Performance. *Phys. Rev. Appl.* **2018**, *9*, 014025.

(12) Hooda, M. K.; Yadav, C. S. Enhanced Thermopower and Low Thermal Conductivity in P-Type Polycrystalline $ZrTe_5$. *Appl. Phys. Lett.* **2017**, *111*, 053902.

(13) Smontara, A.; Biljaković, K. Thermal Properties of $ZrTe_5$. *Mol. Cryst. Liq. Cryst.* **1985**, *121*, 141−144.

(14) Wang, C.; Wang, H.; Chen, Y. B.; Yao, S.-H.; Zhou, J. First-Principles Study of Lattice Thermal Conductivity in $ZrTe_5$ and $HfTe_5$. *J. Appl. Phys.* **2018**, *123*, 175104.

(15) Gorai, P.; Toberer, E. S.; Stevanović, V. Computational Identification of Promising Thermoelectric Materials among Known Quasi-2D Binary Compounds. *J. Mater. Chem. A* **2016**, *4*, 11110−11116.

(16) Lv, Y.-Y.; Zhang, F.; Zhang, B.-B.; Pang, B.; Yao, S.-H.; Chen, Y. B.; Ye, L.; Zhou, J.; Zhang, S.-T.; Chen, Y.-F. Microstructure, Growth Mechanism and Anisotropic Resistivity of Quasi-One-Dimensional $ZrTe_5$ Crystal. *J. Cryst. Growth* **2017**, *457*, 250−254.

(17) Cahill, D. G. Analysis of Heat Flow in Layered Structures for Time-Domain Thermoreflectance. *Rev. Sci. Instrum.* **2004**, *75*, 5119−5122.

(18) Zhu, J.; Tang, D.; Wang, W.; Liu, J.; Holub, K. W.; Yang, R. Ultrafast Thermoreflectance Techniques for Measuring Thermal Conductivity and Interface Thermal Conductance of Thin Films. *J. Appl. Phys.* **2010**, *108*, 094315.

(19) Zhu, J.; Wu, X.; Lattery, D. M.; Zheng, W.; Wang, X. The Ultrafast Laser Pump-Probe Technique for Thermal Characterization of Materials with Micro/Nanostructures. *Nanoscale Microscale Thermophys. Eng.* **2017**, *21*, 177−198.

(20) Eesley, G. L.; Clemens, B. M.; Paddock, C. A. Generation and Detection of Picosecond Acoustic Pulses in Thin Metal Films. *Appl. Phys. Lett.* **1987**, *50*, 717−719.

(21) Thomsen, C.; Grahn, H. T.; Maris, H. J.; Tauc, J. Surface Generation and Detection of Phonons by Picosecond Light Pulses. *Phys. Rev. B: Condens. Matter Mater. Phys.* **1986**, *34*, 4129−4138.

(22) Wang, X. J.; Mori, T.; Kuzmych-Ianchuk, I.; Michiue, Y.; Yubuta, K.; Shishido, T.; Grin, Y.; Okada, S.; Cahill, D. G. Thermal Conductivity of Layered Borides: The Effect of Building Defects on the Thermal Conductivity of $TmAlB_4$ and the Anisotropic Thermal Conductivity of AlB_2. *APL Mater.* **2014**, *2*, 046113.

(23) Zhu, J.; Zhu, Y.; Wu, X.; Song, H.; Zhang, Y.; Wang, X. Structure-Thermal Property Correlation of Aligned Silicon Dioxide Nanorod Arrays. *Appl. Phys. Lett.* **2016**, *108*, 231903.

(24) Shaviv, R.; Westrum, E. F., Jr.; Fjellvåg, H.; Kjekshus, A. $ZrTe_5$ and $HfTe_5$: The Heat Capacity and Derived Thermophysical Properties from 6 to 350 K. *J. Solid State Chem.* **1989**, *81*, 103−111.

(25) Zhao, L.-D.; Lo, S.-H.; Zhang, Y.; Sun, H.; Tan, G.; Uher, C.; Wolverton, C.; Dravid, V. P.; Kanatzidis, M. G. Ultralow Thermal Conductivity and High Thermoelectric Figure of Merit in SnSe Crystals. *Nature* **2014**, *508*, 373−377.

(26) Wei, P.-C.; Bhattacharya, S.; He, J.; Neeleshwar, S.; Podila, R.; Chen, Y. Y.; Rao, A. M. The Intrinsic Thermal Conductivity of SnSe. *Nature* **2016**, *539*, E1−E2.

(27) Lo, C.-W. T.; Ortiz, B. R.; Toberer, E. S.; He, A.; Svitlyk, V.; Chernyshov, D.; Kolodiazhnyi, T.; Lidin, S.; Mozharivskyj, Y. Synthesis, Structure, and Thermoelectric Properties of α-Zn_3Sb_2 and Comparison to β-$Zn_{13}Sb_{10}$. *Chem. Mater.* **2017**, *29*, 5249−5258.

(28) Ainsworth, L. Single Crystal Bismuth Telluride. *Proc. Phys. Soc., London, Sect. B* **1956**, *69*, 606−612.

(29) Walsh, L. A.; Smyth, C. M.; Barton, A. T.; Wang, Q.; Che, Z.; Yue, R.; Kim, J.; Kim, M. J.; Wallace, R. M.; Hinkle, C. L. Interface Chemistry of Contact Metals and Ferromagnets on the Topological Insulator Bi_2Se_3. *J. Phys. Chem. C* **2017**, *121*, 23551−23563.

(30) Cardinal, T.; Devender; Borca-Tasciuc, T.; Ramanath, G. Tailoring Electrical Transport Across Metal-Thermoelectric Interfaces Using a Nanomolecular Monolayer. *ACS Appl. Mater. Interfaces* **2016**, *8*, 4275−4279.

(31) Feser, J. P.; Cahill, D. G. Probing Anisotropic Heat Transport Using Time-Domain Thermoreflectance with Offset Laser Spots. *Rev. Sci. Instrum.* **2012**, *83*, 104901.

(32) Feser, J. P.; Liu, J.; Cahill, D. G. Pump-Probe Measurements of the Thermal Conductivity Tensor for Materials Lacking In-Plane Symmetry. *Rev. Sci. Instrum.* **2014**, *85*, 104903.

(33) Zhu, J.; Park, H.; Chen, J.-Y.; Gu, X.; Zhang, H.; Karthikeyan, S.; Wendel, N.; Campbell, S. A.; Dawber, M.; Du, X.; Li, M.; Wang, J.-P.; Yang, R.; Wang, X. Revealing the Origins of 3D Anisotropic Thermal Conductivities of Black Phosphorus. *Adv. Electron. Mater.* **2016**, *2*, 1600040.

(34) Moore, J.; McElroy, D.; Barisoni, M. Thermal Conductivity Measurements between 78 and 340 K on Aluminum, Iron, Platinum, and Tungsten. *Proceedings of the 6th Conference on Thermal Conductivity*, 1966; pp 737−778.

(35) Liu, J.; Choi, G.-M.; Cahill, D. G. Measurement of the Anisotropic Thermal Conductivity of Molybdenum Disulfide by the Time-Resolved Magneto-Optic Kerr Effect. *J. Appl. Phys.* **2014**, *116*, 233107.

DOI: 10.1021/acsami.8b12504
ACS Appl. Mater. Interfaces 2018, 10, 40740−40747

(36) Fugallo, G.; Cepellotti, A.; Paulatto, L.; Lazzeri, M.; Marzari, N.; Mauri, F. Thermal Conductivity of Graphene and Graphite: Collective Excitations and Mean Free Paths. *Nano Lett.* **2014**, *14*, 6109−6114.
(37) Kuang, Y.; Lindsay, L.; Huang, B. Unusual Enhancement in Intrinsic Thermal Conductivity of Multilayer Graphene by Tensile Strains. *Nano Lett.* **2015**, *15*, 6121−6127.
(38) Hellman, O.; Broido, D. A. Phonon Thermal Transport in Bi_2Te_3 from First Principles. *Phys. Rev. B: Condens. Matter Mater. Phys.* **2014**, *90*, 134309.
(39) Lee, S.; Esfarjani, K.; Luo, T.; Zhou, J.; Tian, Z.; Chen, G. Resonant Bonding Leads to Low Lattice Thermal Conductivity. *Nat. Commun.* **2014**, *5*, 3525.
(40) Xu, B.; Feng, T.; Li, Z.; Pantelides, S. T.; Wu, Y. Constructing Highly Porous Thermoelectric Monoliths with High-Performance and Improved Portability from Solution-Synthesized Shape-Controlled Nanocrystals. *Nano Lett.* **2018**, *18*, 4034−4039.
(41) Bessas, D.; Sergueev, I.; Wille, H.-C.; Perßon, J.; Ebling, D.; Hermann, R. P. Lattice Dynamics in Bi_2Te_3 and Sb_2Te_3: Te and Sb Density of Phonon States. *Phys. Rev. B: Condens. Matter Mater. Phys.* **2012**, *86*, 224301.
(42) Fu, Q.; Yang, J.; Chen, Y.; Li, D.; Xu, D. Experimental Evidence of Very Long Intrinsic Phonon Mean Free Path Along the C-Axis of Graphite. *Appl. Phys. Lett.* **2015**, *106*, 031905.
(43) Kumar, S.; Singh, R. N. Thermal Conductivity of Polycrystalline Materials. *J. Am. Ceram. Soc.* **1995**, *78*, 728−736.
(44) Ditmars, D. A.; Plint, C. A.; Shukla, R. C. Aluminum. I. Measurement of the Relative Enthalpy from 273 to 929 K and Derivation of Thermodynamic Functions for Al(s) from 0 K to Its Melting Point. *Int. J. Thermophys.* **1985**, *6*, 499−515.
(45) Kresse, G.; Hafner, J. Ab Initio Molecular Dynamics for Liquid Metals. *Phys. Rev. B: Condens. Matter Mater. Phys.* **1993**, *47*, 558−561.
(46) Kresse, G.; Furthmüller, J. Efficient Iterative Schemes for Ab Initio Total-Energy Calculations Using a Plane-Wave Basis Set. *Phys. Rev. B: Condens. Matter Mater. Phys.* **1996**, *54*, 11169−11186.
(47) Fjellvåg, H.; Kjekshus, A. Structural Properties of $ZrTe_5$ and $HfTe_5$ as Seen by Powder Diffraction. *Solid State Commun.* **1986**, *60*, 91−93.
(48) Okada, S.; Sambongi, T.; Ido, M.; Tazuke, Y.; Aoki, R.; Fujita, O. Negative Evidences for Charge/Spin Density Wave in $ZrTe_5$. *J. Phys. Soc. Jpn.* **1982**, *51*, 460−467.
(49) Togo, A.; Oba, F.; Tanaka, I. First-Principles Calculations of the Ferroelastic Transition between Rutile-Type and $CaCl_2$-Type SiO_2 at High Pressures. *Phys. Rev. B: Condens. Matter Mater. Phys.* **2008**, *78*, 134106.
(50) Li, W.; Carrete, J.; Katcho, N. A.; Mingo, N. ShengBTE: A Solver of the Boltzmann Transport Equation for Phonons. *Comput. Phys. Commun.* **2014**, *185*, 1747−1758.

DOI: 10.1021/acsami.8b12504
ACS Appl. Mater. Interfaces 2018, 10, 40740−40747

Supporting Information for
Record-Low and Anisotropic Thermal Conductivity of Quasi-One-Dimensional Bulk $ZrTe_5$ Single Crystal

Jie Zhu,[§,⁋,†] Tianli Feng,[‡,‖,†] Scott Mills,[⊥] Peipei Wang,[⊤] Xuewang Wu,[§] Liyuan Zhang,[⊤] Sokrates T. Pantelides,[‡,‖] Xu Du,[⊥] and Xiaojia Wang[§,⁂,*]

[§]Department of Mechanical Engineering, University of Minnesota, Minneapolis, MN 55455, USA

[⁋]Key Laboratory of Ocean Energy Utilization and Energy Conservation of Ministry of Education, Dalian University of Technology, Dalian, Liaoning 116024, China

[‡]Department of Physics and Astronomy and Department of Electrical Engineering and Computer Science, Vanderbilt University, Nashville, Tennessee 37235, USA

[‖]Materials Science and Technology Division, Oak Ridge National Laboratory, Oak Ridge, Tennessee 37831, USA

[⊥]Department of Physics and Astronomy, Stony Brook University, Stony Brook, New York 11794, USA

[⊤]Department of Physics, Southern University of Science and Technology, Shenzhen, Guangdong 518055, China

[⁂]Department of Electrical and Computer Engineering, University of Minnesota, Minneapolis, MN 55455, USA

[†] J. Z. and T. L. F. contributed equally to this paper.

[*]Corresponding author e-mail: wang4940@umn.edu

1. The acoustic impedance calculations

The acoustic impedance is the product of the material's mass density and sound velocity. We obtain the values for Al density,[1] Al sound velocity,[2] and $ZrTe_5$ density[3] from literature studies, while we use the calculated value of $ZrTe_5$ sound velocity from our first-principles calculations. The obtained acoustic impedance of Al is 2.70×10^6 g m^{-3} × 6420 m s^{-1} ≈ 1.73×10^{10} g m^{-3} s^{-1}, while that of $ZrTe_5$ is 6.10×10^6 g m^{-3} × 494 m s^{-1} ≈ 0.30×10^{10} g m^{-3} s^{-1}.

2. Scanning electron microscopic and optical images

We have carried out cross-sectional scanning electron microscope (SEM) imaging as shown in Figure S1. Here the cross-section is created by focused ion beam (FIB) which digs a rectangular pit in the Al-covered $ZrTe_5$ coated by protective Pt layer. And the SEM images the vertical side of the pit, at a 30° angle (Fig. S1a). From the SEM image (Fig. S1b) we see a sharp interface between Al and $ZrTe_5$. Within the contrast of the image, the "smearing" between the two is within ~10 nm, which is much thinner than the thermal probing depth of TDTR method (80~200 nm). We hence conclude that there should be no significant diffusion between Al and $ZrTe_5$. The $ZrTe_5$ crystal shows no lamina-like morphology. The depth of the smooth area shown in the cross-sectional SEM image is large enough for our measurement to use the semi-infinite assumption, since the thermal penetration depth of the TDTR measurements is in the range of 80 to 200 nm. We have also taken a top-view SEM image to illustrate the smooth surface (the *a*-*c* plane) of a bare $ZrTe_5$ crystal (Fig. S1c). Along with the microscopic optical image taken at roughly the same surface area of the bare $ZrTe_5$ crystal (Fig. S1d), we conclude that the samples we prepared for thermal measurements were in good condition without any noticeable degradation or delamination.

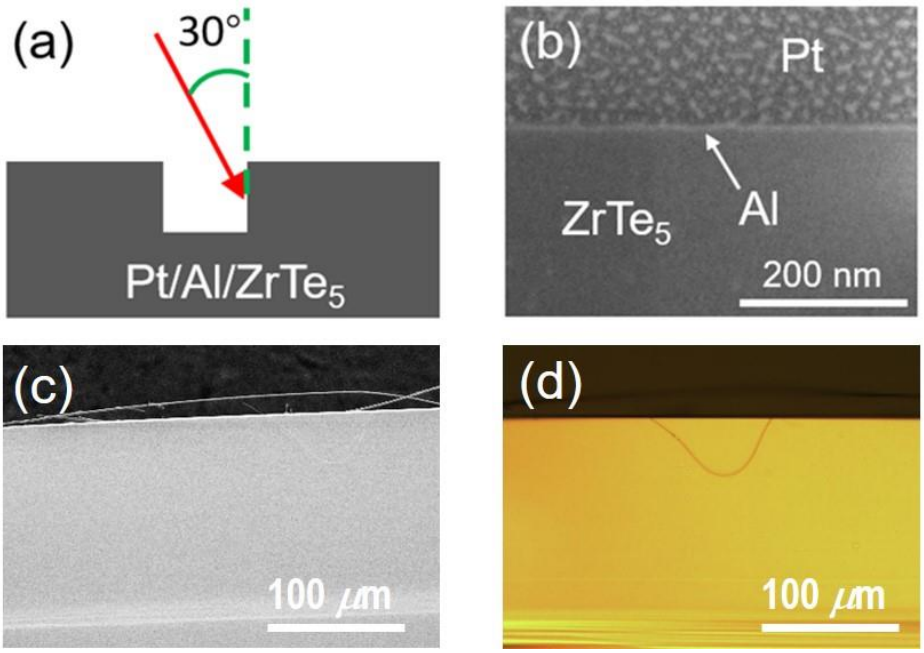

Figure S1. Structural characterization. (a) The red arrow indicates that the cross-sectional SEM image was taken along the direction of 30° from the sample surface normal. (b) The cross-sectional SEM image of Pt/Al/$ZrTe_5$. The thickness of the Al layer is ~20 nm. The spots in the Pt layer were caused by the use of a carbon-based precursor for the deposition of Pt inside of the SEM/FIB, which creates the enhanced contrast. (c) The top-view SEM image of a bare $ZrTe_5$ crystal (the *a*-*c* plane). (d) The optical microscope image of the bare $ZrTe_5$ crystal taken at roughly the same area.

3. Sensitivity analysis of in-plane measurement on $ZrTe_5$

The details for how to analyze the measurement sensitivity by the TDTR method can be found in our previous publication.[4] From the sensitivity analysis results (Fig. S2), we can see the measurement sensitivity to the in-plane thermal conductivity of $ZrTe_5$ along the *a*-axis is calculated as ~0.01 using the experimentally determined in-plane thermal conductivity of $\Lambda_r = \Lambda_a =$ 4 W m^{-1} K^{-1}. This magnitude of sensitivity is close to the bottom line of the TDTR measurements for getting reliable results with an acceptable uncertainty. While for the *c*-axis with an in-plane thermal conductivity of $\Lambda_r = \Lambda_c =$ 1.9 W m^{-1} K^{-1} (from first-principles prediction), the measurement sensitivity is too low to accurately determine the thermal conductivity by fitting the

experimental data. Considering the reasonable agreement in values of Λ_a and Λ_b from both experiments and theoretical modeling, we report the first-principles predicted value for Λ_c.

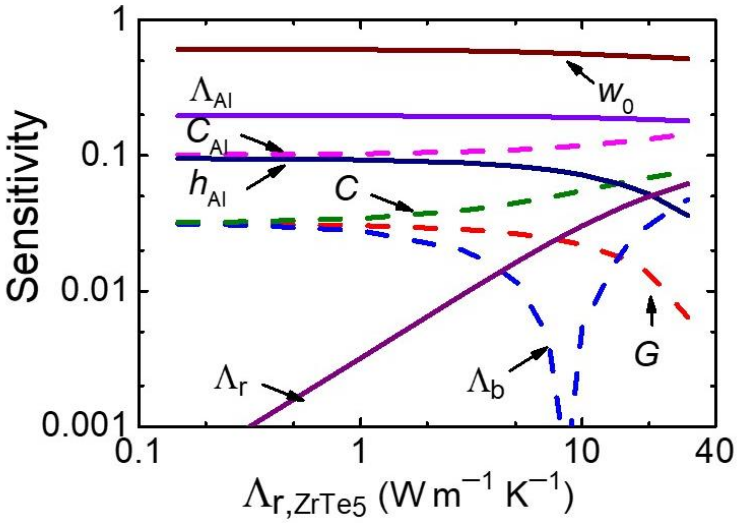

Figure S2. Beam-offset measurement sensitivities to individual parameters. Here, Λ_r is the in-plane thermal conductivity of $ZrTe_5$ (along either the *a*- or *c*-axis), Λ_b is the through-plane thermal conductivity of $ZrTe_5$, Λ_{Al} is the thermal conductivity of Al (isotropic), h_{Al} is the thickness of the Al transducer, w_0 is the beam spot radius, G is the interfacial thermal conductance between Al and $ZrTe_5$, C is the heat capacity of $ZrTe_5$, and C_{Al} is the heat capacity of Al.

4. Convergence study of the first-principles calculations

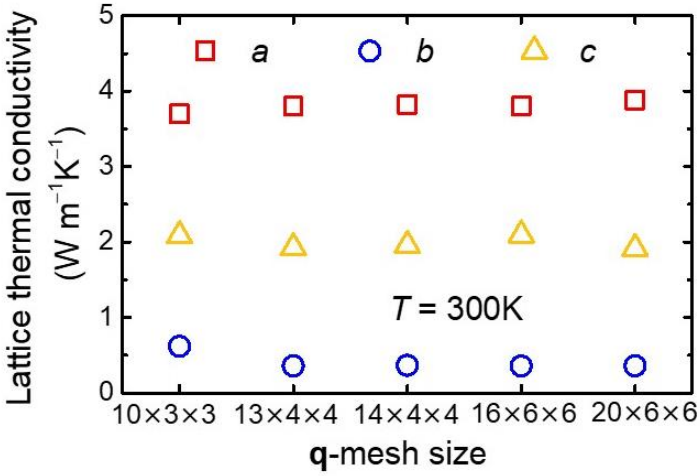

Figure S3. The convergence of lattice thermal conductivity calculation with respect to the size of phonon **q**-mesh.

5. Lists of material parameters used in first-principles calculations

Table S1. Comparison of the Grüneisen parameters of different materials.

Materials	Grüneisen parameter		Λ (W m^{-1} K^{-1})	
	DFT (this work)	Literature	DFT (this work)	Literature
Si	0.44	0.40 ± 0.07[5]*	160	155-165[6,7]*
GaAs	0.69	0.8[8]*	44	46[9,10]*
$ZrTe_5$	1.25		3.8, 0.36, 1.9	
SnSe	1.41	1.26, 1.29, 0.46[11]‡ 1.44, 1.35, 0.64[12]‡	0.68, 1.9, 1.3	0.5-1.8[13]‡, [14-16]*
Bi_2Te_3	1.5	1.50 ± 0.01[17]*	~1.3-2	1.3[18]‡
PbS	1.96		2.2	2.19[19]‡, 2.38[20]*, 2.56[21]*, 2.52[22]*
PbTe, PbSe	~2.1	1.96, 2.23[23]‡	~1.7	2.01, 1.75[23]‡

* experiment, ‡ theory.

Table S2. The lattice constants obtained from different methods.

Methods	*a*	*b*	*c*
	(Å)	(Å)	(Å)
Experiment 10 K[24]	3.9797(6)	14.470(3)	13.676(2)
Experiment 293 K[24]	3.9875(6)	14.530(3)	13.724(2)
Experiment[25]	3.9876	14.5020	13.7270
Experiment[26]	3.974	14.492	13.730
Experiment 150 K[27]	3.78	15.04	14.12
Experiment 298 K[27]	3.86	14.47	13.81
DFT standard (this work)	3.9390	14.2922	13.5106
DFT + Spin-orbital coupling (this work)	3.9398	14.2607	13.5321
DFT + vdW (this work)	4.0364	14.7740	13.8404

References

(1) Predel, B. Ac-Ag ... Au-Zr · Introduction: Datasheet from Landolt-Börnstein - Group IV Physical Chemistry · Volume 12A: "Ac-Ag ... Au-Zr" in SpringerMaterials. In *Phase Equilibria, Crystallographic and Thermodynamic Data of Binary Alloys · Ac-Ag ... Au-Zr*; Predel, B., Ed.; Springer-Verlag Berlin Heidelberg: 2006.

(2) Albanese, G.; Ghezzi, C. Anharmonic Contributions to Elastic and Inelastic Scattering of X Rays at Bragg Reflections in Aluminum. *Phys. Rev. B* **1973,** *8* (4), 1315-1323.

(3) ZrTe5 Crystal Structure: Datasheet from "PAULING FILE Multinaries Edition – 2012" in SpringerMaterials. Villars, P.; Cenzual, K., Eds. Springer-Verlag Berlin Heidelberg & Material Phases Data System (MPDS), Switzerland & National Institute for Materials Science (NIMS), Japan.

(4) Zhu, J.; Park, H.; Chen, J. Y.; Gu, X.; Zhang, H.; Karthikeyan, S.; Wendel, N.; Campbell, S. A.; Dawber, M.; Du, X. Revealing the Origins of 3D Anisotropic Thermal Conductivities of Black Phosphorus. *Adv. Electron. Mater.* **2016,** *2* (5), 1600040.

(5) Gauster, W. B. Low-Temperature Grüneisen Parameters for Silicon and Aluminum. *Phys. Rev. B* **1971,** *4* (4), 1288-1296.

(6) Abeles, B.; Beers, D. S.; Cody, G. D.; Dismukes, J. P. Thermal Conductivity of Ge-Si Alloys at High Temperatures. *Phys. Rev.* **1962,** *125* (1), 44-46.

(7) Glassbrenner, C. J.; Slack, G. A. Thermal Conductivity of Silicon and Germanium from 3 K to the Melting Point. *Phys. Rev.* **1964,** *134* (4A), A1058-A1069.

(8) Adachi, S. *GaAs and Related Materials: Bulk Semiconducting and Superlattice Properties*, World Scientific: 1994.

(9) Ng, K. K. *Complete Guide to Semiconductor Devices*, Wiley Online Library: 2002.

(10) Sze, S. *Physics of Semiconductor Devices*, 2nd ed.; John Wiley & Sons: New York, 1981.

(11) Liu, G.; Zhou, J.; Wang, H. Anisotropic Thermal Expansion of SnSe from First-Principles Calculations Based on Grüneisen's Theory. *Phys. Chem. Chem. Phys.* **2017,** *19* (23), 15187-15193.

(12) Bansal, D.; Hong, J.; Li, C. W.; May, A. F.; Porter, W.; Hu, M. Y.; Abernathy, D. L.; Delaire, O. Phonon Anharmonicity and Negative Thermal Expansion in SnSe. *Phys. Rev. B* **2016,** *94* (5), 054307.

(13) Carrete, J.; Mingo, N.; Curtarolo, S. Low Thermal Conductivity and Triaxial Phononic Anisotropy of SnSe. *Appl. Phys. Lett.* **2014,** *105* (10), 101907.

(14) Zhao, L.-D.; Lo, S.-H.; Zhang, Y.; Sun, H.; Tan, G.; Uher, C.; Wolverton, C.; Dravid, V. P.; Kanatzidis, M. G. Ultralow Thermal Conductivity and High Thermoelectric Figure of Merit in SnSe Crystals. *Nature* **2014,** *508*, 373.

(15) Sassi, S.; Candolfi, C.; Vaney, J.-B.; Ohorodniichuk, V.; Masschelein, P.; Dauscher, A.; Lenoir, B. Assessment of the Thermoelectric Performance of Polycrystalline P-Type SnSe. *Appl. Phys. Lett.* **2014,** *104* (21), 212105.

(16) Chen, C.-L.; Wang, H.; Chen, Y.-Y.; Day, T.; Snyder, G. J. Thermoelectric Properties of P-Type Polycrystalline SnSe Doped with Ag. *J. Mater. Chem. A* **2014,** *2* (29), 11171-11176.

(17) Bessas, D.; Sergueev, I.; Wille, H. C.; Perßon, J.; Ebling, D.; Hermann, R. P. Lattice Dynamics in Bi_2Te_3 and Sb_2Te_3: Te and Sb Density of Phonon States. *Phys. Rev. B* **2012,** *86* (22), 224301.

(18) Hellman, O.; Broido, D. A. Phonon Thermal Transport in Bi_2Te_3 from First Principles. *Phys. Rev. B* **2014,** *90* (13), 134309.

(19) Wei, L.; Chen, J.-f.; He, Q.-y.; Teng, W. Study of Lattice Thermal Conductivity of PbS. *J. Alloy. Compd.* **2014,** *584*, 381-384.
(20) Johnsen, S.; He, J.; Androulakis, J.; Dravid, V. P.; Todorov, I.; Chung, D. Y.; Kanatzidis, M. G. Nanostructures Boost the Thermoelectric Performance of PbS. *J. Am. Chem. Soc.* **2011,** *133* (10), 3460-3470.
(21) Zhao, L.-D.; Lo, S.-H.; He, J.; Li, H.; Biswas, K.; Androulakis, J.; Wu, C.-I.; Hogan, T. P.; Chung, D.-Y.; Dravid, V. P.; Kanatzidis, M. G. High Performance Thermoelectrics from Earth-Abundant Materials: Enhanced Figure of Merit in PbS by Second Phase Nanostructures. *J. Am. Chem. Soc.* **2011,** *133* (50), 20476-20487.
(22) Pei, Y.-L.; Liu, Y. Electrical and Thermal Transport Properties of Pb-Based Chalcogenides: PbTe, PbSe, and PbS. *J. Alloy. Compd.* **2012,** *514*, 40-44.
(23) Zhang, Y.; Ke, X.; Chen, C.; Yang, J.; Kent, P. R. C. Thermodynamic Properties of PbTe, PbSe, and PbS: First-Principles Study. *Phys. Rev. B* **2009,** *80* (2), 024304.
(24) Fjellvåg, H.; Kjekshus, A. Structural Properties of $ZrTe_5$ and $HfTe_5$ as Seen by Powder Diffraction. *Solid State Commun.* **1986,** *60* (2), 91-93.
(25) Okada, S.; Sambongi, T.; Ido, M.; Tazuke, Y.; Aoki, R.; Fujita, O. Negative Evidences for Charge/Spin Density Wave in $ZrTe_5$. *J. Phys. Soc. Jpn.* **1982,** *51* (2), 460.
(26) Littleton, R. T., IV; Tritt, T. M.; Kolis, J. W.; Ketchum, D. R. Transition-Metal Pentatellurides as Potential Low-Temperature Thermoelectric Refrigeration Materials. *Phys. Rev. B* **1999,** *60* (19), 13453-13457.
(27) Littleton, R. T., IV; Tritt, T. M.; Kolis, J. W.; Ketchum, D. R.; Lowhorn, N. D.; Korzenski, M. B. Suppression of the Resistivity Anomaly and Corresponding Thermopower Behavior in the Pentatelluride System by the Addition of Sb: $Hf_{1-X}Zr_XTe_{5-Y}Sb_Y$. *Phys. Rev. B* **2001,** *64* (12), 121104.